

PAPER • OPEN ACCESS

## Dynamic loss and magnetization loss of HTS coated conductors, stacks, and coils for high-speed synchronous machines

To cite this article: Hongye Zhang *et al* 2020 *Supercond. Sci. Technol.* **33** 084008

View the [article online](#) for updates and enhancements.

### You may also like

- [Dynamic resistance and dynamic loss in a ReBCO superconductor](#)  
Hongye Zhang, Boyang Shen, Xiaoyuan Chen *et al.*
- [Dynamic resistance and total loss in a three-tape REBCO stack carrying DC currents in perpendicular AC magnetic fields at 77 K](#)  
Yueming Sun, Jin Fang, Gennady Sidorov *et al.*
- [Modelling of electromagnetic loss in HTS coated conductors over a wide frequency band](#)  
Hongye Zhang, Min Yao, Kevin Kails *et al.*

# Dynamic loss and magnetization loss of HTS coated conductors, stacks, and coils for high-speed synchronous machines

Hongye Zhang , Philip Machura , Kevin Kails , Hongyi Chen  and Markus Mueller

School of Engineering, University of Edinburgh, Edinburgh EH9 3JL, United Kingdom

E-mail: [Hongye.Zhang@ed.ac.uk](mailto:Hongye.Zhang@ed.ac.uk) and [Markus.Mueller@ed.ac.uk](mailto:Markus.Mueller@ed.ac.uk)

Received 30 March 2020, revised 13 May 2020

Accepted for publication 9 June 2020

Published 9 July 2020



## Abstract

Dynamic loss is an essential parameter to consider for the design of high temperature superconducting (HTS) synchronous machine windings. For aerospace electric propulsion systems, the fundamental frequency component and harmonics in electric machines can attain kHz level because of the high rotating speed. However, for HTS coated conductors (CC), the existing definition of dynamic loss only considers the HTS layer, the validity of which at high frequencies is questionable. Besides, the variation of dynamic loss and magnetization loss under skin effect due to high frequency is still unknown. Additionally, the influence of shielding effects among distinct turns on the dynamic loss of HTS stacks and coils remains unclear. In response to the above concerns, by use of the  $H$ -formulation based numerical multilayer modelling method which considers all layers of a CC, the frequency dependence of dynamic loss and magnetization loss of HTS CCs, stacks and coils over a wide range up to 20 kHz has been investigated. Results show that the existing definition of the dynamic region is no longer valid at kHz level, which shrinks rapidly with increasing frequency and magnetization loss plays a progressively important role due to skin effect. Meanwhile, the shielding effect in HTS stacks and coils can enhance the significance of dynamic loss. This paper clarifies the characteristics of dynamic loss and magnetization loss of HTS CCs, stacks, and coils over a wide frequency band, which can serve as a useful reference for accurate loss controlling of machine windings in future aerospace HTS propulsion systems.

Keywords: aerospace propulsion system, dynamic loss, magnetization loss, high frequency, skin effect, shielding effect

(Some figures may appear in colour only in the online journal)

## 1. Introduction

High power density electric motors and generators at MW-scale are the key enablers for future aerospace electric

propulsion systems [1–3]. High temperature superconducting (HTS) technology has provided a possibility for more compact and lighter electric machines with a higher efficiency [4, 5]. Aerospace generators and motors operate at very high speeds (7–50 kRPM), and thus the superconductors in HTS machines ought to be capable of functioning in high-frequency magnetic fields ( $\sim 0.2$ –2 kHz) [5].

Dynamic resistance and dynamic loss have attracted much attention in recent years because they are essential to evaluate the performance of HTS coated conductors (CC) applied in



Original content from this work may be used under the terms of the [Creative Commons Attribution 4.0 licence](https://creativecommons.org/licenses/by/4.0/). Any further distribution of this work must maintain attribution to the author(s) and the title of the work, journal citation and DOI.

HTS magnets, machine windings as well as flux pumps, etc [6–15]. Dynamic loss is generated when a superconductor carrying a direct current (DC) is exposed to an alternating current (AC) magnetic field, of which the analytical expressions have been presented in [12–15] and proven to be in good accordance with experimental measurements. However, it should be pointed out that, the existing definition of dynamic loss only considers the HTS layer of a CC, and neglects the influence of the copper stabilizers, silver overlayer, as well as the substrate. Besides, current dynamic loss measurements were usually conducted at low frequencies no more than 120 Hz [6–8, 12–18].

Magnetization loss is the power dissipation due to an externally applied AC magnetic field of a superconductor carrying no transport current [8], which is mainly composed of hysteresis loss and eddy current loss at high frequencies. As illustrated in [8], the total AC loss is contributed by both dynamic loss and magnetization loss. In our previous research work, AC transport current and magnetization losses of one single HTS CC over a wide frequency band up to 1 MHz have been analyzed [19]. It has been concluded that, when the frequency of the externally applied AC magnetic field is higher than 100 Hz, the loss contributions of the copper stabilizers, silver overlayer and substrate have to be taken into account. Furthermore, the skin effect plays a progressively important role with the increase in frequency [19]. Therefore, for now, it is unclear whether the definition and analytical formulas for dynamic loss are still applicable towards high frequencies at kHz level. Besides, under skin effect, compared with magnetization loss, it should be investigated whether dynamic loss remains an essential concern for the design of high-speed propulsion machines. More importantly, machine windings are usually manufactured in the form of coils. The shielding effect among different turns can affect loss distributions, which should be studied systematically as well.

In response to the above issues, on the basis of [19], the frequency dependence of dynamic loss and magnetization of HTS CCs, stacks, as well as coils over a wide range, from 100 Hz to 20 kHz, has been explored. Firstly, the variation of the dynamic region with frequency for a single CC has been studied. It shows that the existing analytical methods for quantifying dynamic loss are no longer valid at high frequencies, thus the  $\mathbf{H}$ -formulation based numerical multilayer modelling method has been adopted here. This modelling method considers the real structure of every single CC, namely two copper stabilizers, one HTS layer, one silver overlayer, and the substrate. Then, the variation of dynamic loss and magnetization loss with frequency for HTS CCs, stacks, circular and racetrack coils have been investigated respectively. The influence of skin effect and shielding effect on dynamic loss and magnetization loss have been discussed in detail, especially for HTS stacks and coils. Multiple simulation results have been verified by published experimental measurements. Finally, the contributions of dynamic loss and magnetization loss to the total loss of HTS CCs, stacks, as well as coils have been discussed and some crucial conclusions have been drawn.

This paper systematically studies the variation of dynamic loss and magnetization loss for HTS CCs, stacks, circular and

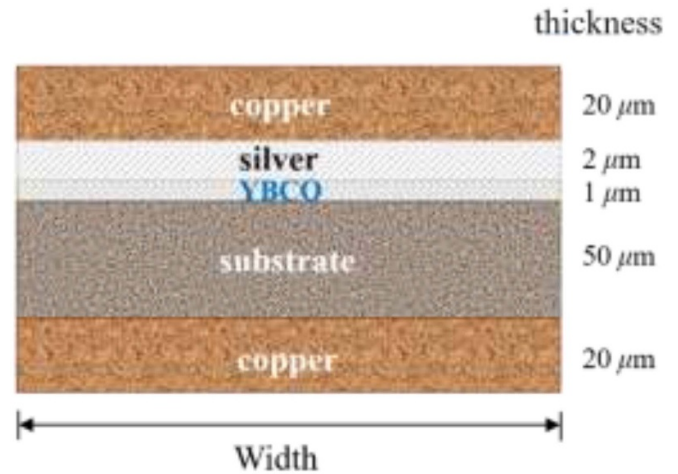


**Figure 1.** The multilayer structure of a typical HTS CC manufactured by SuperPower, Inc.

racetrack coils towards high frequencies of kHz level, at 77 K in liquid nitrogen. Results can be used to predict the electromagnetic performance of HTS windings in high-speed electric machines, which can serve as a useful reference for the design of future aerospace electric propulsion systems.

## 2. Dynamic region with frequency

The  $\mathbf{H}$ -formulation based numerical modelling method mentioned in [19–21] has been adopted in this paper, which is a multilayer model considering the physical structure of HTS CCs, as shown in figure 1. In other words, all layers of an HTS CC, including one HTS layer, two copper stabilizers, one silver overlayer, as well as one substrate, have been taken into account. The used numerical multilayer model has been validated experimentally in [19] with the experimental data presented in [22].

According to Maxwell's equations, Constitutive Law, and Ohm's Law, the general form of  $\mathbf{H}$ -formulation can be written as [19, 23]

$$\frac{1}{\sigma} \nabla \times (\nabla \times \mathbf{H}) + \mu_0 \mu_r \frac{\partial \mathbf{H}}{\partial t} = 0 \quad (1)$$

where  $\mathbf{H}$  represents the magnetic field intensity,  $\mu_0$  denotes the free space permeability,  $\sigma$  and  $\mu_r$  are the conductivity and the relative permeability of the studied material, respectively.

As far as the HTS layer is concerned, we have the  $\mathbf{E}$ - $\mathbf{J}$  power law [24]

$$\|\mathbf{E}\| = E_0 \left( \frac{\|\mathbf{J}\|}{J_c(B)} \right)^n \quad (2)$$

where  $\mathbf{E}$  is the electric field,  $\mathbf{J}$  is the current density along the width of the CC,  $E_0$  is a constant with  $E_0 = 10^{-4} \text{ V m}^{-1}$ , and  $n$  is the power index.  $J_c(B)$  describes the field dependence of

critical current, as (3) [25].

$$J_c = \frac{J_{c0}}{\left(1 + \sqrt{\frac{k^2 \|\mathbf{B}_{\parallel}\|^2 + \|\mathbf{B}_{\perp}\|^2}{B_0}}\right)^{\alpha}} \quad (3)$$

$$\frac{E_0}{J_{c0}^n} \left(1 + \mu_0 \mu_r \sqrt{\frac{k^2 \|\mathbf{H}_{\parallel}\|^2 + \|\mathbf{H}_{\perp}\|^2}{B_0}}\right)^{\alpha n} \cdot \|\nabla \times \mathbf{H}\|^{n-1} \cdot \nabla \times (\nabla \times \mathbf{H}) + \mu_0 \mu_r \frac{\partial \mathbf{H}}{\partial t} = 0 \quad (4)$$

where  $J_{c0}$  is the self-field critical current density,  $\mathbf{B}_{\parallel}$  and  $\mathbf{B}_{\perp}$  are the parallel and perpendicular components of the local magnetic flux density with respect to the wide surface of the CC, respectively.  $B_0$ ,  $k$  and  $\alpha$  are material-related parameters.

On the basis of (1), (2) and (3), the governing equation for the HTS layer can be written as (4), inside which  $\mathbf{H}_{\parallel}$  and  $\mathbf{H}_{\perp}$  are respectively the parallel and perpendicular components of the local magnetic field intensity. It should be underlined that in this paper, we consider that the  $\mathbf{E}\text{-}\mathbf{J}$  power law is valid in the frequency range studied, up to 20 kHz. The physical structure of the studied HTS CC is composed of 5 layers, thus for each layer, the AC loss per unit time (W) can be written as

$$Q_m = 2Lf \int_{1/12f}^{1/f} \int_{S_m} \mathbf{E} \cdot \mathbf{J} dS_m dt \quad (5)$$

where  $L$  means the length of the CC,  $f$  is the AC frequency of the externally applied magnetic field, and  $S_m$  is the cross-sectional area of the  $m$ -th layer, with  $m = 1, 2, 3, 4, 5$ .

Therefore, the total loss per unit time for the whole HTS CC can be obtained as

$$Q_{\text{tot}} = \sum_{m=1}^5 Q_m \quad (6)$$

In our modelling, the HTS CC is surrounded by air and a Dirichlet boundary condition is used. More details can be found in [19].

### 2.1. Dynamic region at low frequencies

When an HTS CC carrying a DC is exposed to an AC magnetic field, its central part with a width of  $2iw$  will be occupied by the DC transport current [12–14], which is named as the dynamic region. Here,  $i$  is the load ratio between the transport current,  $I_t$ , and the self-field critical current (*i.e.* the critical current with no externally applied magnetic field),  $I_{c0}$ , with  $i = I_t/I_{c0}$ .  $2w$  is the width of the HTS CC. Therefore, the dynamic loss per unit time (W),  $Q_{\text{dyn}}$ , can be expressed as

$$Q_{\text{dyn}} = hLf \int_0^{1/f} \int_{(1-i)w}^{(1+i)w} E J dy dt \quad (7)$$

where  $h$ ,  $L$ , and  $2w$  are the thickness, length, and width of the HTS layer, respectively.

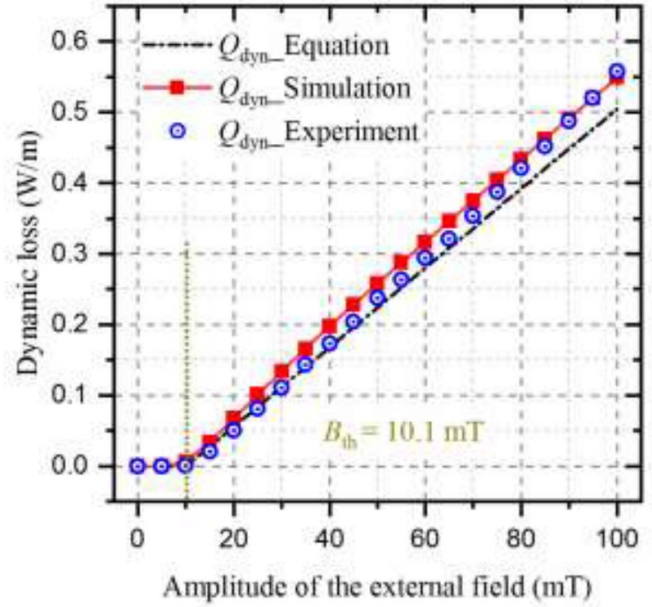


**Figure 2.** Analytical, simulated and measured dynamic loss of the HTS CC sample under varying  $B_{\text{ext}}$  from 0–100 mT.  $I_{c0} = 105.3$  A at 77 K.  $n = 22.5$ . The frequency of the AC magnetic field  $f = 26.62$  Hz.

According to [13, 14, 26], dynamic loss (W) can also be formulated by

$$Q_{\text{dyn}} = \frac{4wfLI_t^2}{I_{c0}} (B_{\text{ext}} - B_{\text{th}}) \quad (8)$$

where  $B_{\text{ext}}$  is the amplitude of the external magnetic flux density, and  $B_{\text{th}}$  is the threshold field, with [27]

$$B_{\text{th}} = \frac{\mu_0 J_{c0} h}{2\pi} \left[ \frac{1}{i} \ln \left( \frac{1+i}{1-i} \right) + \ln \left( \frac{1-i^2}{4i^2} \right) \right] \quad (9)$$

Taking the tested HTS CC sample in [13] as an example,  $I_{c0} = 105.3$  A at 77 K, and  $n = 22.5$ . When the load ratio is 0.5 and the AC frequency of the magnetic field is 26.62 Hz, the simulated dynamic loss calculated by (7) with the  $\mathbf{H}$ -formulation based numerical model, the analytical results obtained by (8), and the experimental data have been depicted together in figure 2.

It can be seen that the simulated  $Q_{\text{dyn}}$  is in good agreement with the analytical and experimental results. On the basis of the simulation, the magnetic flux density and current density along the width of the HTS layer have been presented in figure 3. It can be found that, with the growth of  $B_{\text{ext}}$ , the amount of traversing magnetic flux during one AC cycle (shaded area) and the electric field increase accordingly, leading to the rise of  $Q_{\text{dyn}}$ , which agrees well with [13]. At low frequencies, *e.g.* 26.62 Hz, the dynamic region to effectively carry DC transport current is determined by  $2iw$ .

### 2.2. Dynamic region at high frequencies

The validity of the adopted  $\mathbf{H}$ -formulation based numerical multilayer modelling method over a wide frequency band has

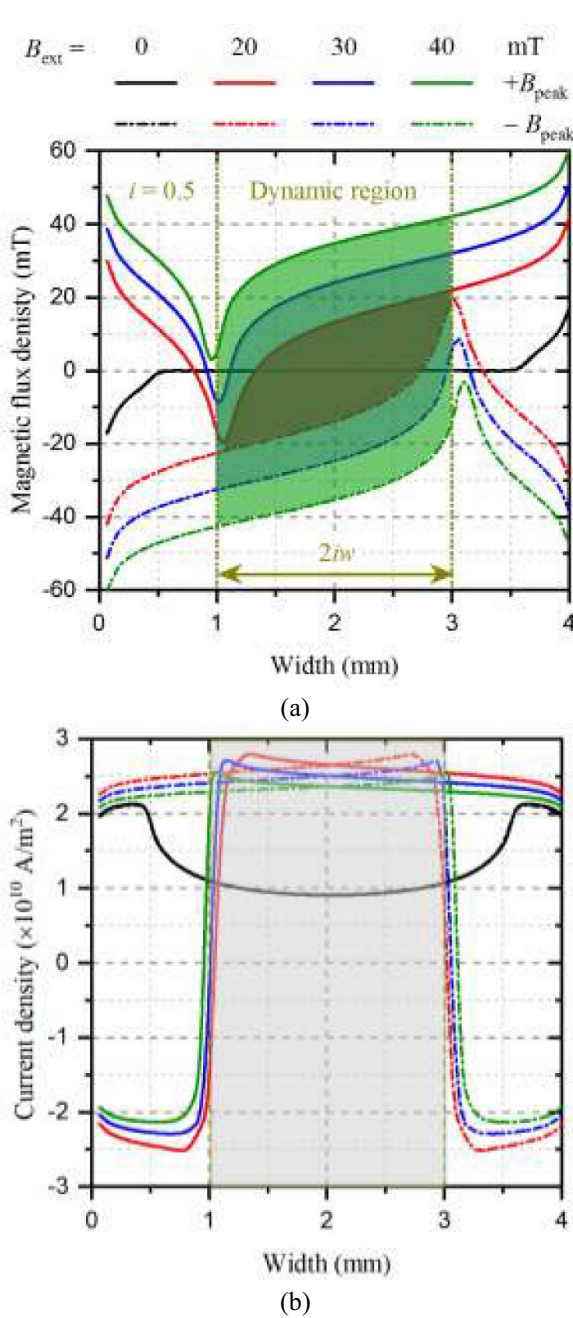


**Figure 3.** The magnetic flux density and current density profiles along the width of the HTS CC at the moment of  $\pm$  peak field, under different external magnetic fields. Load ratio  $i = 0.5$ , and  $B_{\text{ext}}$  varies between 0–40 mT. (a) Magnetic flux density profiles. (b) Current density profiles.

been discussed in [19]. Taking the tested CC sample with a magnetic substrate in [22] as an example, the simulated transport current losses in different layers and measured results under distinct frequencies up to 15 kHz, have been shown in figure 4. It can be seen that the simulated total transport current loss,  $Q_{\text{tot. Simu.}}$ , agrees well with the experimental data,  $Q_{\text{tot. Expe.}}$ . Also, as mentioned in [19], most loss occurs in the copper stabilizers when  $f$  exceeds 300 Hz because of the skin effect and the influence of the magnetic substrate.

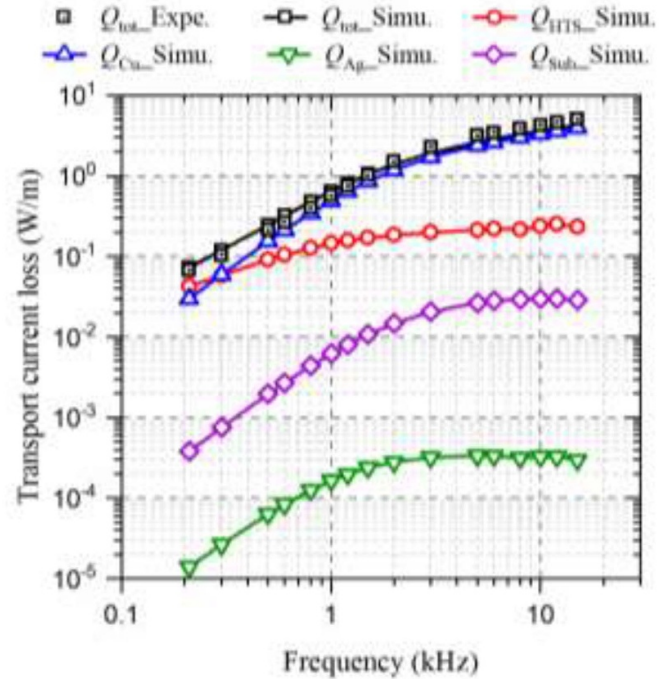


**Figure 4.** The simulated and measured AC transport current losses of the tested HTS CC mentioned in [22].  $I_{c0} = 108$  A at 77 K,  $I_t = 45$  A,  $n = 30$ , and  $f$  varies from 210 Hz to 15 kHz.

with the  $\mathbf{H}$ -formulation based numerical model, the studied HTS CC with a non-magnetic substrate in [19] has been considered here, with  $I_{c0} = 99.23$  A at 77 K and  $n = 38$ . The magnetic flux density and current density profiles in its HTS layer have been presented in figure 5. It can be seen that, the amount of traversing magnetic flux during one AC cycle shrinks rapidly with increasing frequency, as well as the width of the dynamic region. In other words, the width of the dynamic region cannot be determined by  $2iw$  at high frequencies above 1 kHz, which in reality increases inversely with frequency. Additionally, the dynamic loss of the HTS layer during one cycle decreases with frequency, which however disagrees with (8). According to (8), dynamic loss per unit time should be in a linear correlation with frequency, which means that the dynamic loss generated during one AC cycle should be independent of the frequency of external magnetic fields. Therefore, (8) is inapplicable for high frequencies at kHz level and above. To quantify the dynamic loss in high-speed machines, numerical models are thus recommended. According to [8], dynamic loss per unit time (W) for a single CC or a stack can be calculated by

$$Q_{\text{dyn}} = 2LN_t I_t f \cdot \int_{1/2f}^{1/f} \frac{1}{S} \int_S E(t) dS dt \quad (10)$$

where  $S$  is the total cross-sectional area of the HTS layers, and  $N_t$  is the total number of CCs.

However, for a coil composed of a number of CCs, the electric field distribution is tightly related to the direction of the externally applied magnetic field. Thus, for calculating dynamic loss per unit time  $Q_{\text{dyn}}$  (W), the average electric field

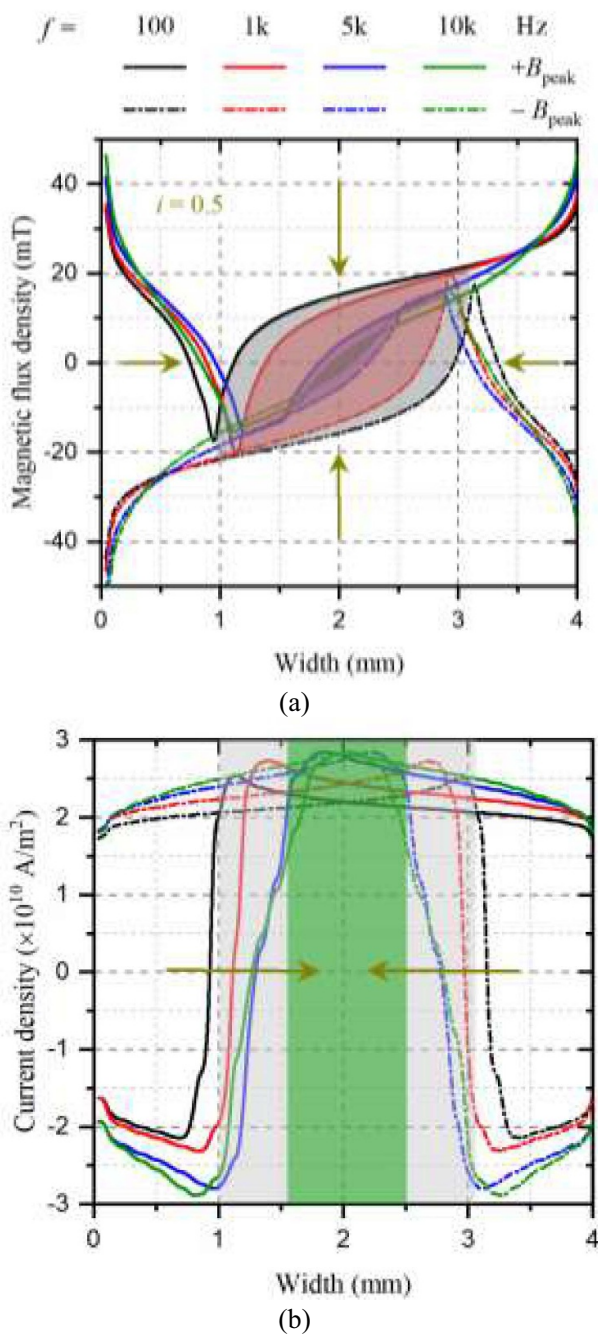


**Figure 5.** The magnetic flux density and current density profiles along the width of the HTS CC at the moment of  $\pm$  peak field, under varying magnetic fields, of which  $f$  ranges from 100 Hz—10 kHz. Load ratio  $i = 0.5$ .  $B_{\text{ext}} = 20$  mT. (a) Magnetic flux density profiles. (b) Current density profiles.

in the whole volume of the coil needs to be considered, as

$$Q_{\text{dyn}} = 2L_{\text{avg}}N_t I f \cdot \int_{1/2f}^{1/f} \frac{1}{V} \int_V E(t) dV dt \quad (11)$$

where  $V$  is the total volume of the HTS layers, and  $L_{\text{avg}}$  represents the average length of the studied coil.

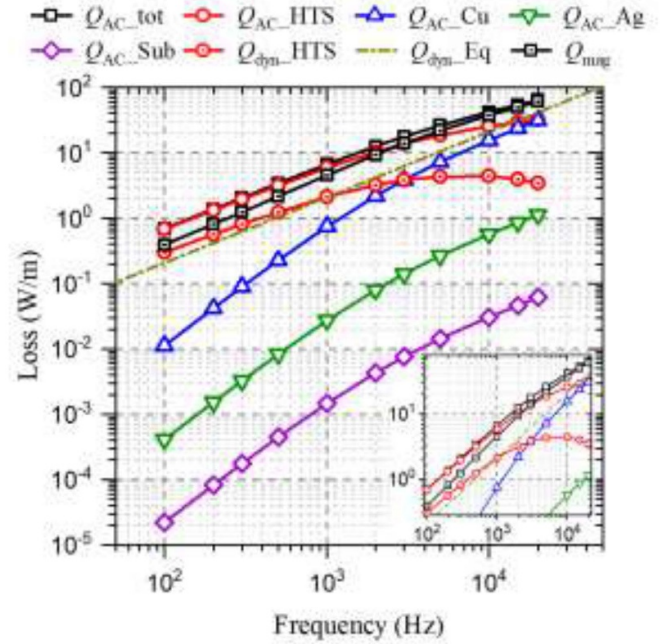


**Figure 6.** Variation of AC losses in different layers, dynamic loss and magnetization loss with frequency for the HTS CC with  $I_{c0} = 99.23$  A at 77 K.  $f$  ranges from 100 Hz—30 kHz.  $i = 0.5$ .  $B_{\text{ext}} = 20$  mT.

### 3. Variation of dynamic loss and magnetization loss with frequency

#### 3.1. Single HTS CC

For the same HTS CC discussed in section 2.2, the simulated AC losses,  $Q_{\text{AC}}$ , in different layers, dynamic loss,  $Q_{\text{dyn}}$ , in the HTS layer, as well as magnetization loss,  $Q_{\text{mag}}$ , with varying frequency from 100 Hz to 20 kHz have been depicted together in figure 6. Besides, the analytical  $Q_{\text{dyn}}$  obtained by (8) has also been presented.

It can be found that, at low frequencies below 1 kHz, more than 90% of the total loss is concentrated in the HTS layer; however, with the growth of frequency, the loss in the copper stabilizers increase rapidly and goes over that of the HTS layer at 20 kHz. This phenomenon of loss redistribution is because of the skin effect [19], as shown in figure 7. The magnetic flux density will be driven to both ends of the HTS CC, as well as its outer copper stabilizers. Therefore, at high frequencies, magnetization loss plays a dominant role, e.g. at 10 kHz,  $Q_{\text{mag}}$  accounts for 90% of the total AC loss,  $Q_{\text{AC\_tot}}$ . Compared with the HTS layer and copper stabilizers, the losses in the silver overlayer and substrate are always negligible, because they are inner layers and do not possess a high electrical conductivity that can be compared to that of the HTS layer.

It should be underlined that, dynamic loss per unit time begins to decrease from 10 kHz, i.e. dynamic loss during one AC cycle increases inversely with frequency, which is in good accordance with figure 5. In addition, the simulated  $Q_{\text{dyn\_HTS}}$  clearly differs from the analytical results calculated by (8) at

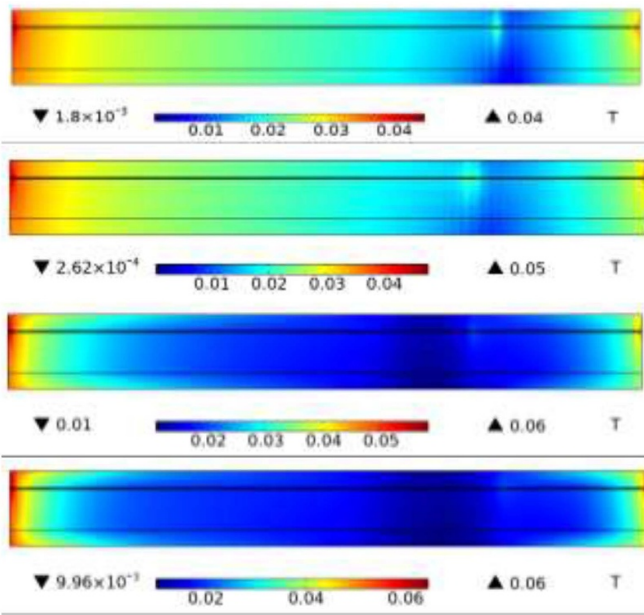


**Figure 7.** The magnetic flux density distribution in the cross-section of the HTS CC at the phase of  $3/2\pi$ , under different frequencies. From top to bottom,  $f$  is 100 Hz, 1 kHz, 10 kHz, and 20 kHz, respectively. Load ratio  $i = 0.5$ .  $B_{ext} = 20$  mT.

high frequencies, especially for  $f$  greater than 1 kHz. Therefore, as mentioned in section 2.2, (8) is inapplicable for high frequencies above 1 kHz.

According to figure 6, it seems that dynamic loss only accounts for one small fraction (less than 50%) of the total AC loss, which is actually related to load ratio  $i$  and the amplitude of the externally applied magnetic field,  $B_{ext}$ . Figure 8 shows the correlation between the loss ratio,  $Q_{dyn}/Q_{AC\_tot}$ , and load ratio  $i$  under distinct  $f$ . It can be found that, in general, for the same  $i$  and  $B_{ext}$ ,  $Q_{dyn}/Q_{AC\_tot}$  decreases rapidly with frequency. Taking  $i = 0.8$  and  $B_{ext} = 100$  mT as an example, when  $f$  increases from 100 Hz to 20 kHz,  $Q_{dyn}/Q_{AC\_tot}$  drops dramatically from 95% to around 3.3%. In fact, as analysed before, when  $f$  goes beyond 1 kHz, the transport current and magnetic flux will be pushed to both ends and outer copper stabilizers of the HTS CC due to skin effect, leading to a fast rise of magnetization loss.

$Q_{dyn}/Q_{AC\_tot}$  is in a positive correlation with  $i$ , as it determines directly the width of the dynamic region. Besides, the existence of DC transport current is the key difference between dynamic loss and magnetization loss as far as their generation mechanism is concerned. Therefore, a higher DC load ratio results in a higher  $Q_{dyn}/Q_{AC\_tot}$ .

As shown in figure 8, at low frequencies, e.g.  $f = 100$  Hz,  $Q_{dyn}/Q_{AC\_tot}$  increases positively with  $B_{ext}$ . However, when  $f$  turns higher, e.g.  $f > 1$  kHz,  $Q_{dyn}/Q_{AC\_tot}$  begins to decrease with increasing  $B_{ext}$ . Actually, at low frequencies, as shown in figure 3, a higher  $B_{ext}$  means more magnetic flux traversing the HTS CC, thus a higher dynamic loss is generated. At high frequency, under the influence of skin effect, magnetization loss plays a dominant role. In this case, as shown in figure 7, most magnetic flux will be concentrated in both ends of

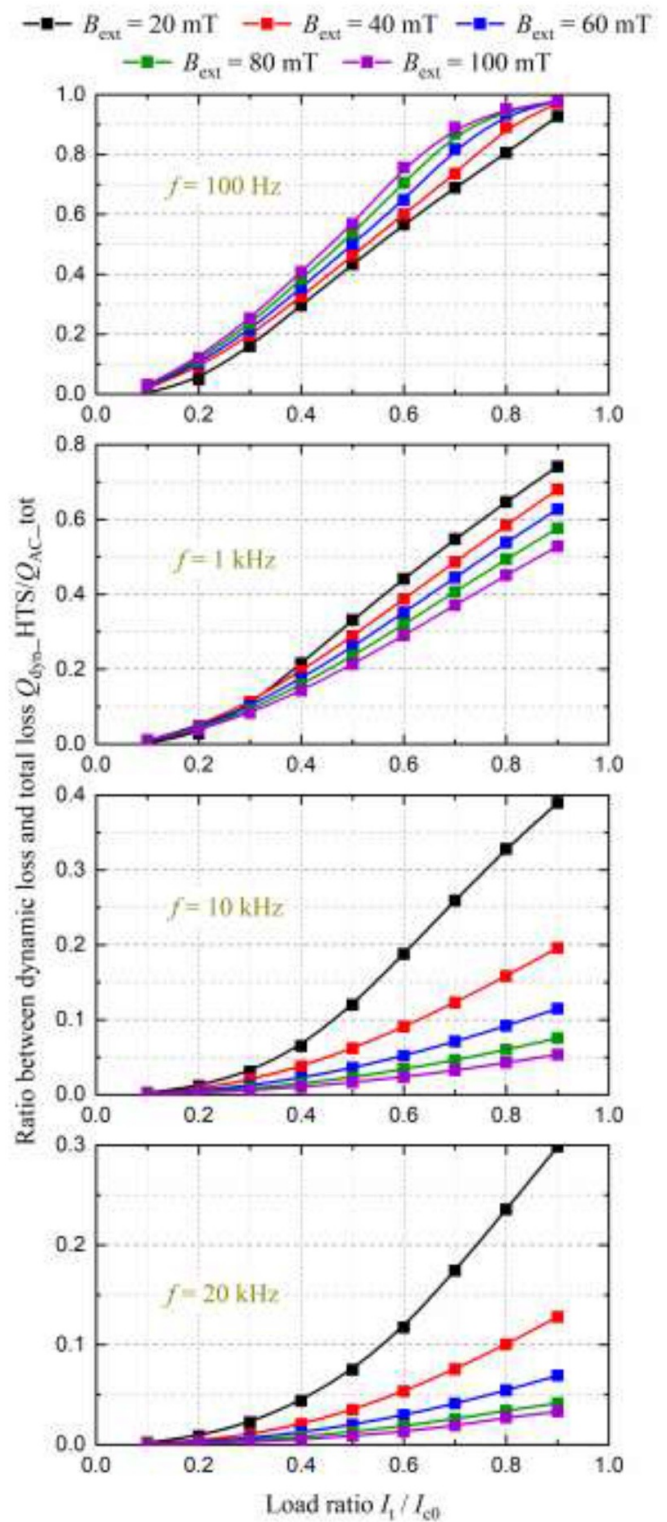


**Figure 8.** The correlation between loss ratio  $Q_{dyn\_HTS}/Q_{AC\_tot}$  and load ratio  $i$  under distinct external magnetic fields for different frequencies.  $i$  varies from 0.1 to 0.9, and magnetic flux density ranges from 20 mT to 100 mT. From top to bottom,  $f$  is 100 Hz, 1 kHz, 10 kHz, and 20 kHz, respectively.

the HTS CC, thus a higher  $B_{ext}$  means more magnetization loss generated on the two sides of the CC. To conclude, the

amplitude of the external magnetic field has different influence on  $Q_{\text{dyn}}/Q_{\text{AC\_tot}}$  with different frequencies. At low frequencies below 1 kHz, a higher  $B_{\text{ext}}$  contributes to a higher  $Q_{\text{dyn}}$ ; however, at higher frequencies above 1 kHz, a higher  $B_{\text{ext}}$  brings about a higher  $Q_{\text{mag}}$ .

Through the above analyses, it can be confirmed that, at low frequencies, dynamic loss is an essential parameter to consider for the design of HTS magnets, low-speed machines (*e.g.* ultra-low-speed wind-farm generators at  $\sim 10$  RPM, and low-speed motors for ship propulsion at 100–250 RPM), as well as flux pump devices, etc. For instance, as shown in figure 8, at 100 Hz, when  $B_{\text{ext}}$  is greater than 40 mT and  $i$  is above 0.6,  $Q_{\text{dyn}}$  accounts for more than 60% of the total loss. When  $i$  attains 0.8,  $Q_{\text{dyn}}$  can become more than 80% of the total loss even under a small  $B_{\text{ext}}$  like 20 mT. However, when it comes to HTS high-speed synchronous machines with a rotational speed higher than 7 kRPM, the skin effect should also be accounted for, because high-frequency magnetic fields appear in such cases. For example, at  $f = 1$  kHz, when  $i$  reaches 0.8 and  $B_{\text{ext}}$  gets 80 mT,  $Q_{\text{dyn}}$  is equal to  $Q_{\text{mag}}$ , both of which account for half of the total loss. In this case, dynamic loss and magnetization loss are both significant to be considered. If harmonics with higher frequency components above 1 kHz are to be included, magnetization loss deserves more attention.

### 3.2. HTS stack

In most HTS applications, to acquire a high current-carrying capacity, stacks or coils composed of many turns of HTS CCs are preferred and more practical. Therefore, in this section, the variation of dynamic loss and magnetization loss with frequency in a stack of HTS coils have been investigated. The 2D numerical model for a stack is an expansion of the multilayer model of one single HTS CC.

At first, to validate the 2D stack numerical models, the parameters of the tested stack of 15 HTS tapes in [28] have been adopted here. For every single tape,  $I_{c0} = 150$  A at 77 K,  $n = 36$ , and  $B_0 = 0.21$  T. The thickness of the insulation between tapes is around  $60 \mu\text{m}$ . The transport current loss calculated by the  $\mathbf{H}$ -formulation based 2D multilayer stack models and experimental data have been depicted together in figure 9. It can be seen that the simulation agrees well with the experimental measurements. Additionally, at low frequencies below 100 Hz, the loss in the HTS layer,  $Q_{\text{HTS}}$ , accounts for more than 95% of the total loss,  $Q_{\text{tot}}$ , which is in good accordance with figure 6 and [19].

Then, in order to better show the differences between one single CC and a stack of CCs with respect to  $Q_{\text{dyn}}$  and  $Q_{\text{mag}}$ , the parameters of the studied HTS tape in section 3.1 have been adopted. With this stack numerical model, the variation of  $Q_{\text{dyn}}$  and  $Q_{\text{mag}}$  with frequency has been investigated. Load ratio  $i$  is set to 0.5,  $B_{\text{ext}}$  has been chosen as 20 mT, and  $f$  ranges from 100 Hz to 20 kHz.

Figure 10 shows the magnetic flux density and current density distribution in the HTS stack under different frequencies when  $B_{\text{ext}} = 20$  mT and  $i = 0.5$ . It can be seen that, with the increase of frequency, both the magnetic flux and transport current will be driven to both ends of the stack, due to skin

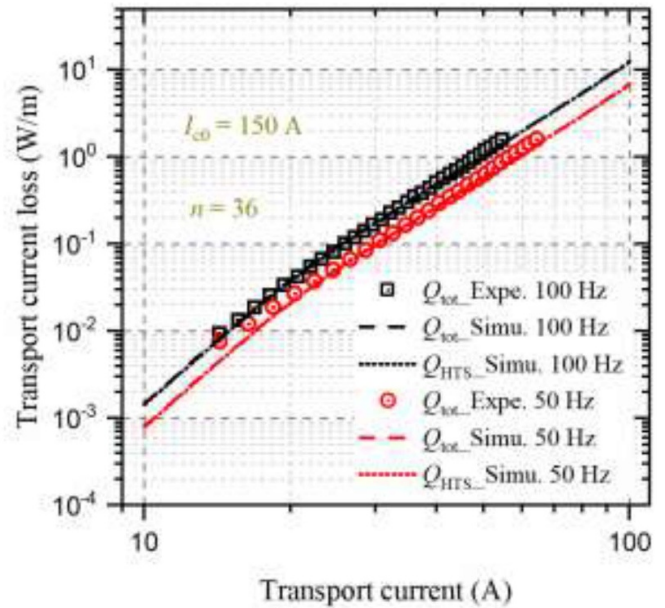
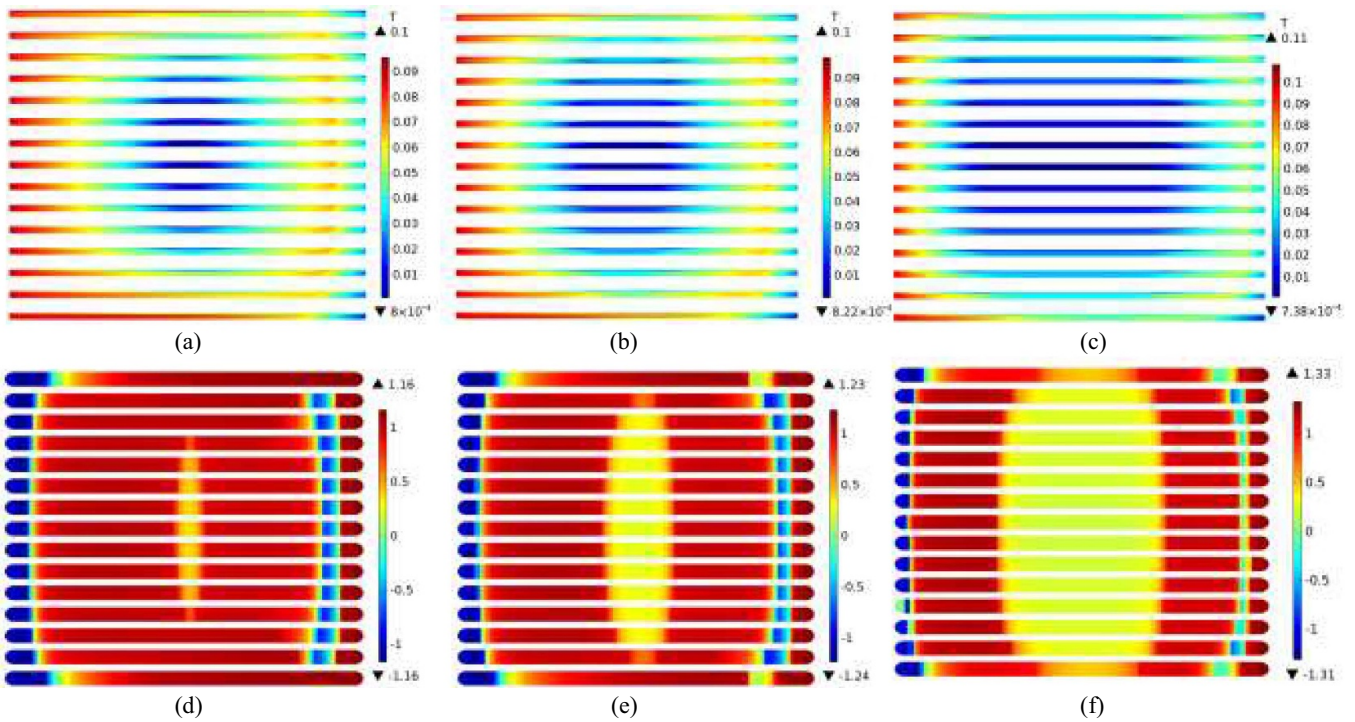


**Figure 9.** The simulated and measured transport current loss of the stack of 15 HTS CCs carrying varying AC transport current. The amplitude of the AC current varies from 10 to 100 A, and  $f$  has been chosen as 50 Hz and 100 Hz.

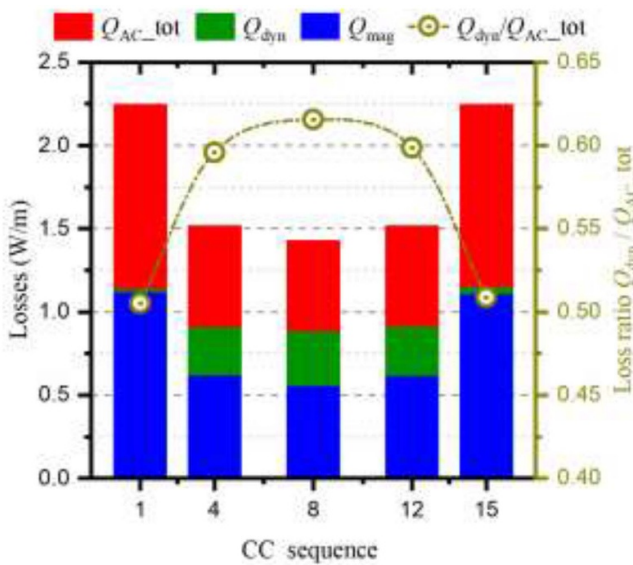
effect, as mentioned in section 3.1. In addition, it appears that the skin effect is more influential to the HTS CCs in the centre of the stack. In fact, because of the shielding effects of the external CCs on the internal ones, less magnetic flux can penetrate in the middle part of the stack, as shown in (a), (b) and (c). Therefore, in general,  $J_c(B)$  of the internal CCs is relatively higher than that of the external ones, leading to a lower  $J/J_c(B)$  in the middle part of the stack, as shown in (d), (e) and (f). To conclude, under both skin effect and shielding effect, at highest frequencies, the highest flux density and current density appear at both ends of the outermost CCs in an HTS stack, and they are in a positive correlation with frequency.

Figure 11 shows the total loss, dynamic loss and magnetization loss in 5 distinct CCs of the stack when  $f = 1$  kHz. The 5 CCs are the first, fourth, eighth, twelfth, and fifteenth tape, respectively. It can be seen that, more losses are generated in the outermost CCs, namely the first and fifteenth tapes, which is in good accordance with the conclusions drawn from figure 10. Besides, the loss ratio  $Q_{\text{dyn}}/Q_{\text{AC\_tot}}$  is the highest for the most middle CC because, as it is shielded by the outer turns, reducing the magnetisation loss. Therefore, at high frequencies, *e.g.*  $f = 1$  kHz, dynamic loss can still play a dominant role in the middle parts of the HTS stack.

Figure 12 shows the frequency dependence of dynamic loss and magnetization loss for the HTS stack. It can be found that, when  $f$  is less than 10 kHz, the loss generated in the HTS layer accounts for the majority of the total loss. However, when  $f$  becomes greater than 10 kHz, most of the loss is concentrated in the copper stabilizers, which is due to skin effect, as mentioned in section 3.1. For frequencies lower than 3 kHz, dynamic loss dominates the total loss, but when  $f$  rises above 3 kHz, magnetization loss contributes more to the total loss



**Figure 10.** Magnetic flux density and current density distribution in the studied stack of 15 HTS CCs.  $B_{ext} = 20$  mT,  $I_t = 49.5$  A, and  $f$  varies from 100 Hz to 10 kHz. (a), (b) and (c) represent the magnetic flux density distribution at the phase of  $3\pi/2$  for  $f = 100$  Hz, 1 kHz, and 10 kHz, respectively. (d), (e) and (f) show  $J/J_c$  in the HTS layer at the phase of  $2\pi$  for  $f = 100$  Hz, 1 kHz, and 10 kHz, respectively. For a better image effect, the thickness of each HTS CC has been adjusted accordingly.



**Figure 11.** Total loss, dynamic loss and magnetization loss of the 1st, 4th, 8th, 12th and 15th CC in the HTS stack, when  $f = 1$  kHz,  $B_{ext} = 20$  mT, and  $I_t = 49.5$  A.

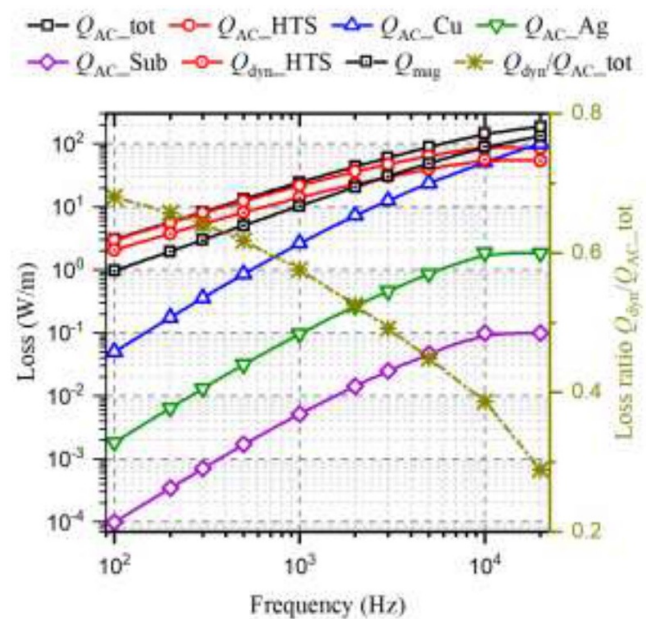


**Figure 12.** Variation of AC losses in different layers, dynamic loss magnetization loss, and loss ratio  $Q_{dyn}/Q_{AC\_tot}$  with frequency for the HTS stack composed of 15 CCs.  $f$  ranges from 100 Hz to 20 kHz.  $i = 0.5$ .  $B_{ext} = 20$  mT.

and dynamic loss begins to decrease from 10 kHz. Therefore, with increasing frequency, the AC loss generated in the copper stabilizers,  $Q_{AC\_Cu}$ , will be approaching  $Q_{mag}$  as well as  $Q_{AC\_tot}$ . In this case, the magnetic flux and transport current will be driven to both ends of each CC and its outer copper parts, as shown in figure 10.

It should be noted that, the HTS stack is composed of the same CC as discussed in section 3.1. Comparing figures 12 and 6, it is interesting to note that, in figure 6 the dynamic loss of one single CC is always less than the magnetization loss under

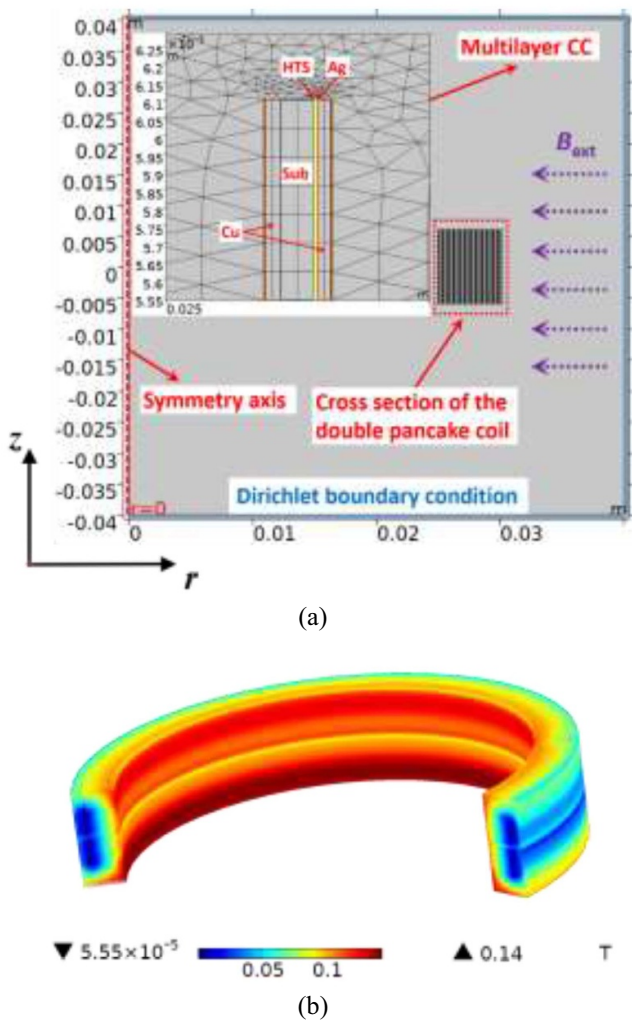


**Figure 13.** 2D coil model layout and 3D magnetic flux density distribution of the double pancake coil.  $f = 1$  kHz. (a) Cross-section of the 2D model.  $B_{ext}$  is along the  $r$ -axis in the cylindrical coordinate system and perpendicular to the wide surfaces of the CCs. (b) Flux density distribution of the coil.

different frequencies, from 100 Hz to 30 kHz. However, at the same  $B_{ext}$ ,  $i$ , and frequency range, the magnetization loss of the HTS stack does not exceed the dynamic loss until 3 kHz in figure 12. In fact, as mentioned before, this difference is due to the shielding effect of the outer CCs on the middle ones, thus dynamic loss can still play a dominant role when  $f$  is below 3 kHz. However, when  $f$  continues to increase, because of skin effect, magnetization loss will increase rapidly. Therefore, the loss ratio  $Q_{dyn}/Q_{AC\_tot}$  reduces with frequency, from 68% at 100 Hz to 29% at 20 kHz. To conclude, at high frequencies, we need to consider both the skin effect and shielding effect for the loss quantification of an HTS stack. Compared with a single CC, the influence of dynamic loss in a stack is more significant.

### 3.3. HTS coil

The 2D modelling of HTS stacks can be a convenient way to reflect the electromagnetic properties of the cross-section

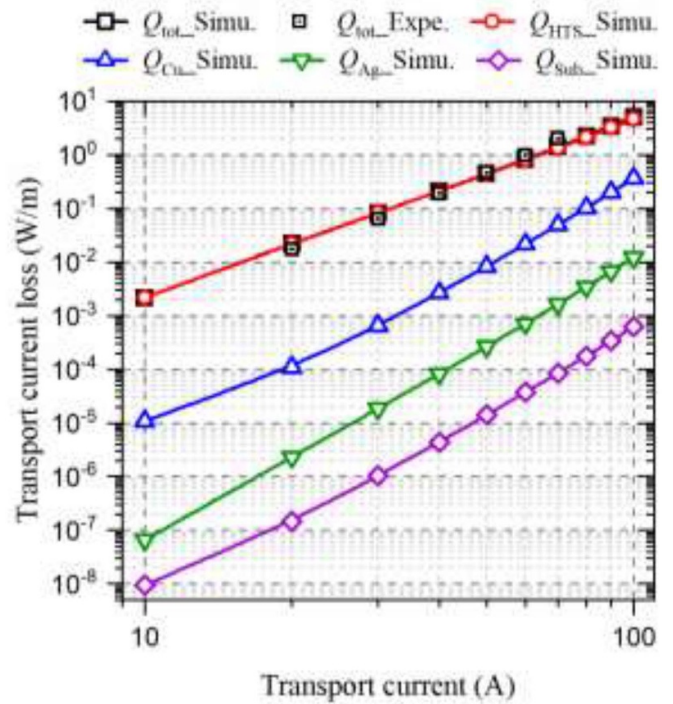


**Figure 14.** The simulated and measured transport current loss of the  $2 \times 18$  double pancake circular coils. The amplitude of the AC current varies from 10 to 100 A, and  $f = 100$  Hz.

of a number of turns of HTS CCs. However, as far as one HTS coil is concerned, when the ratio between its thickness and diameter cannot be neglected, we have to consider the shape of the studied coil to accurately quantify the loss characteristics. Therefore in this section, the frequency dependence of dynamic loss and magnetization loss in a circular and a racetrack coil have been explored, respectively.

**3.3.1 Circular coil.** HTS circular coils are important elements for superconducting magnets. The tested  $2 \times 18$  circular double pancake coil in [29] have been referenced here, which was fabricated from 6 mm wide SuperPower SCS6050 CCs. The inner diameter of the coil is 50 mm, and its KAPTON insulation thickness is  $100 \mu\text{m}$ . The self-field critical current of the single CC is 115 A at 77 K.

Given that the circular coil is both centrosymmetric and axisymmetric, its numerical model has been built with a 2D method based on  $\mathbf{H}$ -formulation [29, 30]. However, unlike [29] which only models the HTS layer of the CC, the coil modelling in this paper has been conducted considering the multilayer structure of each single CC, as shown in figure 13(a). Similar to our previous modelling method for a single tape in [19], the Dirichlet boundary condition has been chosen for applying external magnetic fields. Considering that  $J_c(B)$  is primarily determined by the perpendicular component  $B_{\perp}$ , as shown in (3), the direction of the external magnetic field has been chosen to be perpendicular to the wide surface of the CCs and parallel to the cross-section of the coil, with the field intensity  $H_r = B_{ext}/\mu_0 \cdot \sin(2\pi r/t)$ .

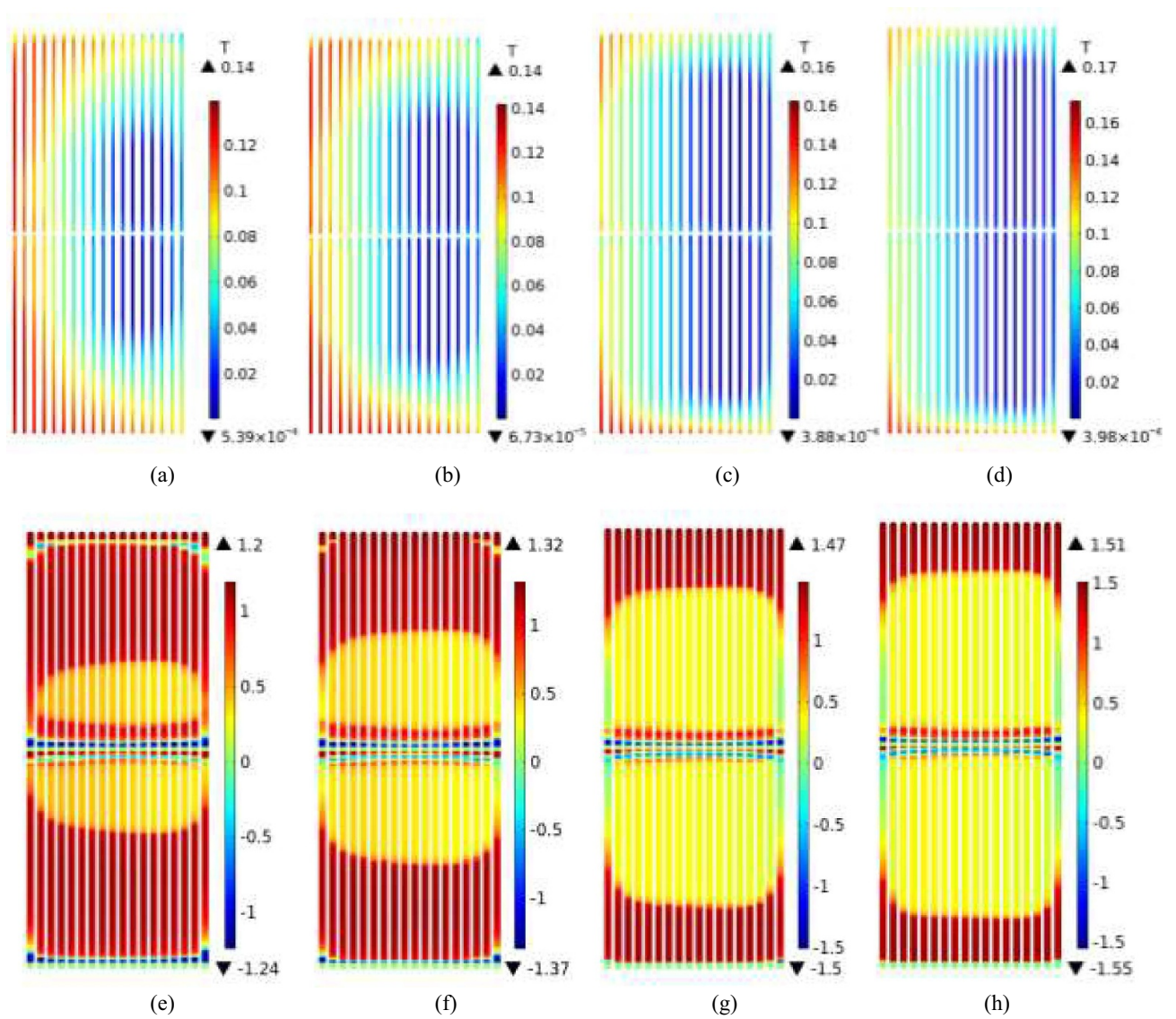


**Figure 15.** Magnetic flux density and current density distribution in the cross-section of the studied  $2 \times 18$  double pancake coil.  $B_{\text{ext}} = 50$  mT, for each tape  $I_t = 60$  A, and  $f$  varies from 100 Hz to 20 kHz. (a), (b), (c) and (d) represent the magnetic flux density distribution at the phase of  $3\pi/2$  for  $f = 100$  Hz, 1 kHz, 10 kHz, and 20 kHz respectively. (e), (f), (g) and (h) show  $J/J_c$  in the HTS layer at the phase of  $2\pi$  for  $f = 100$  Hz, 1 kHz, 10 kHz, and 20 kHz respectively. For a better image effect, the thickness of each HTS CC has been adjusted accordingly.

with this 2D numerical multilayer model, the simulated transport current loss and experimental data of this double pancake coil are depicted together in figure 14, both of which agree well with each other. Then, through this numerical model for the same double pancake circular coil, the variation of dynamic loss and magnetization loss with frequency from 100 Hz to 20 kHz has been investigated. Load ratio  $i$  has been chosen as 0.5, and  $B_{\text{ext}}$  is set to 50 mT. Figure 13(b) presents the 3D magnetic flux density distribution of the double pancake coil at the phase of  $3\pi/2$  with  $f = 1$  kHz.

Figure 15 shows the magnetic flux density and current density distribution in the cross-section of the double pancake coil when  $f$  varies from 100 Hz to 20 kHz. It can be seen that, in general, the magnetic flux and current have a symmetrical distribution in the two coils, and both the highest flux density and current density increase with frequency. Similar to

the case of stacks, due to skin effect, the magnetic flux and current have been pushed to the upper and lower borders of the pancake coil with increasing frequency. Like the shielding effect of the external CCs on the internal ones for a stack, here the coil shows the same trend. However, according to (a), (b), (c) and (d), it appears that the innermost turns have a shielding effect over the external parts. It has to be clarified that, the phenomenon that a large amount of magnetic flux has been concentrated in the internal turns is because of the high self fields generated by the coil, parallel to the wide surface of the CCs, rather than the shielding effect among different CCs. The critical current density  $J_c(B)$  is determined by both the parallel and perpendicular field components, thus in (e) and (f)  $J/J_c(B)$  of the internal turns is generally higher than that of the external ones. However,  $J_c(B)$  is mainly decided by the perpendicular field that is largely

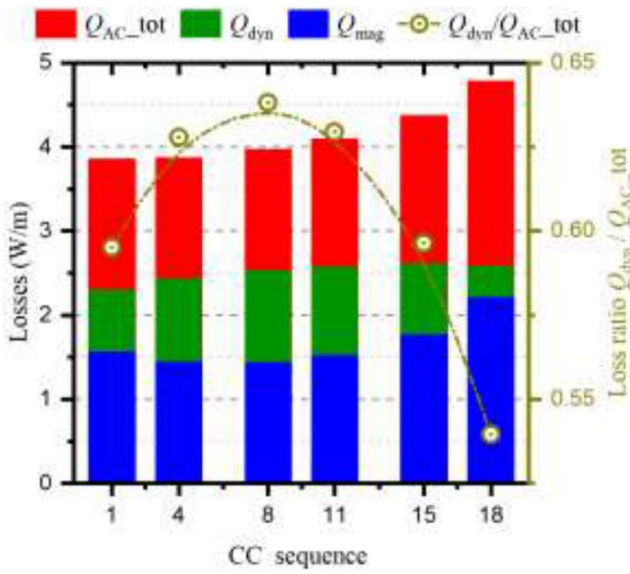


**Figure 16.** Total loss, dynamic loss and magnetization loss of the 1st, 4th, 8th, 11th, 15th, and 18th CC (from inside to outside) in the HTS coil, when  $f = 1$  kHz,  $B_{\text{ext}} = 50$  mT, and  $i = 0.5$ .

determined by the externally applied magnetic field, so the difference regarding  $J/J_c(B)$  between internal and external parts is not significant. Especially, at high frequencies, this difference has been weakened by the skin effect, as shown in (g) and (h).

To better describe the shielding effect of the innermost and outermost turns over the middle parts, the total loss, dynamic loss and magnetization loss in 6 distinct double turns of the coil have been presented in figure 16, with  $f = 1$  kHz. The 6 turns are the first, fourth, eighth, eleventh, fifteenth and eighteenth double turns, respectively. It can be seen that, the total loss for each double turn increases from inside to outside. More magnetization loss has been produced in the outermost turns, because they have a shielding effect on the middle parts, as mentioned before, leading to a higher dynamic loss in the middle turns. Therefore, the loss ratio  $Q_{\text{dyn}}/Q_{\text{AC\_tot}}$  attains the highest at the 8th turn and becomes the smallest at the 18th. However, it needs to be pointed out that, even at high frequencies, *e.g.*  $f = 1$  kHz, dynamic loss can still dominate the total power dissipation, which is different from the case of a single CC, as shown in figure 8. Therefore, combined with figure 11, we can conclude that, because of the shielding effect of the outermost CCs on the middle parts, the influence of dynamic loss has been increased in a stack or a coil.

Figure 17 describes the frequency dependence of the AC losses in different layers, dynamic loss as well as magnetization loss over the cross-section of the double pancake coil. In general, figure 17 shows the same trend as figure 12, that both the total loss and magnetization loss increase rapidly with frequency due to skin effect, and the loss generated in the copper stabilizers exceeds that of the HTS layer when  $f$  turns greater than 15 kHz. Although the proportion of dynamic loss over the total loss is decreasing rapidly, from 74% at 100 Hz to 32% at 20 kHz, it is still above 50% within the frequency range below

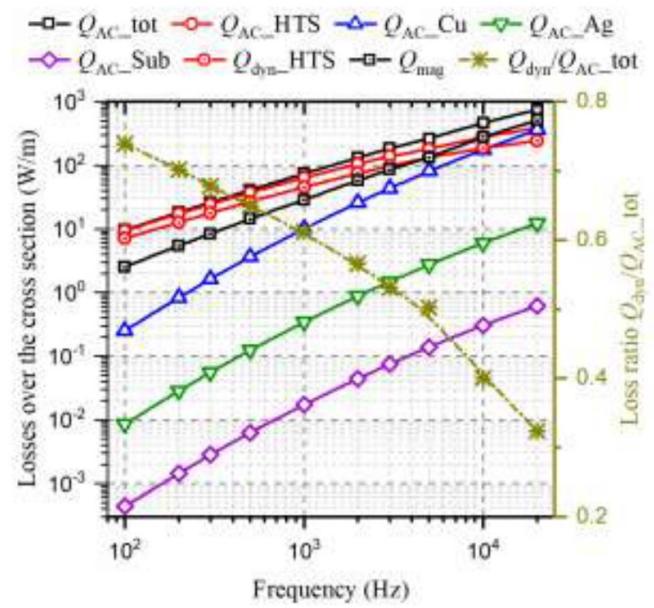


**Figure 17.** Variation of AC losses in different layers, dynamic loss magnetization loss, and loss ratio  $Q_{\text{dyn}}/Q_{\text{AC\_tot}}$  with frequency for the double pancake HTS coil.  $f$  ranges from 100 Hz to 20 kHz.  $i = 0.5$ .  $B_{\text{ext}} = 50$  mT.

3 kHz. Therefore, as concluded in section 3.2, both dynamic loss and magnetization loss need to be taken into account for characterizing the electromagnetic performance of HTS coils operated at the kHz level.

**3.3.2 Racetrack coil.** HTS racetrack coils are widely adopted as superconducting machine windings. To accurately quantify the loss characteristics of a racetrack coil, a 3D numerical model is necessary, especially when the ratio between its thickness and diameter cannot be neglected. 3D modelling of HTS racetrack coils has been discussed in [25, 31] with a homogenization method. Although the homogenization method can greatly save computing time, it cannot be used for studying the frequency dependence of losses in different layers of the HTS CC.

On the basis of the homogenized model in [25, 31], a 3D numerical model for the racetrack coil taking into account the multilayer structure of each CC has been built in this paper, as shown in figure 18. It should be underlined here that, to reduce the computation complexity, it is reasonable to model only one part of the coil considering its central and axial

symmetry. However, to study dynamic loss, AC external magnetic field needs to be applied so that the continuity of current flow or magnetic flux in certain boundaries has to be guaranteed. In this section, the direction of the externally applied magnetic field has been chosen to be perpendicular to the wide surface of CCs in the straight part, along the  $x$ -axis, with  $H_x = B_{\text{ext}}/\mu_0 \cdot \sin(2\pi ft)$ . Therefore, we have modelled only half of the circular part and one-quarter of the straight part as far as one coil is concerned. Different boundary conditions have to be applied separately: to keep the continuity of current flow, zero flux has been chosen for current input

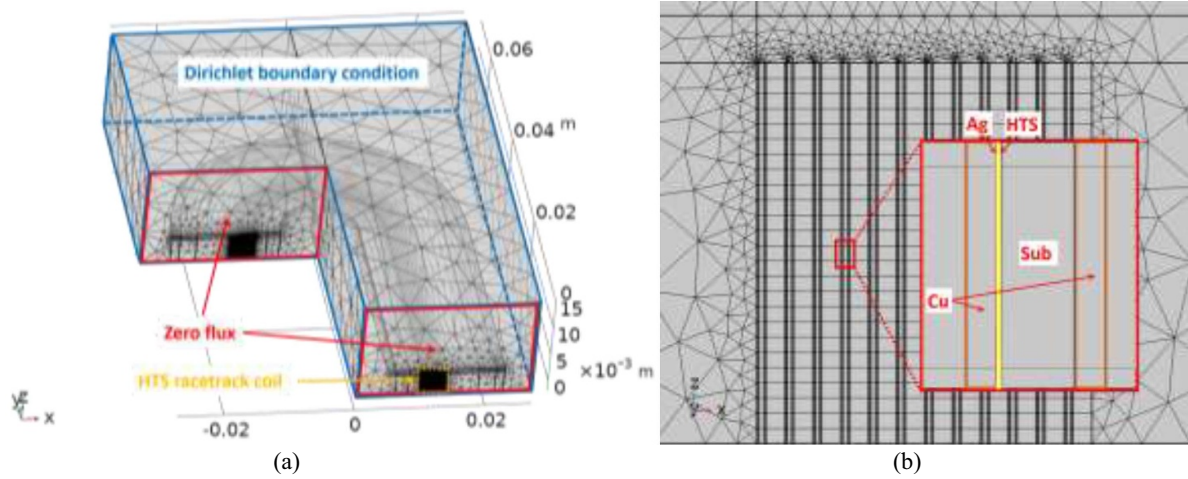


**Figure 18.** 3D numerical multilayer model of the HTS racetrack double pancake coil taking into account the physical structure of each CC, in which only one-eighth of the straight part and one-quarter of the circular section have been shown. (a) Whole mesh view and boundary condition. (b) Meshing of the cross-section of one coil.

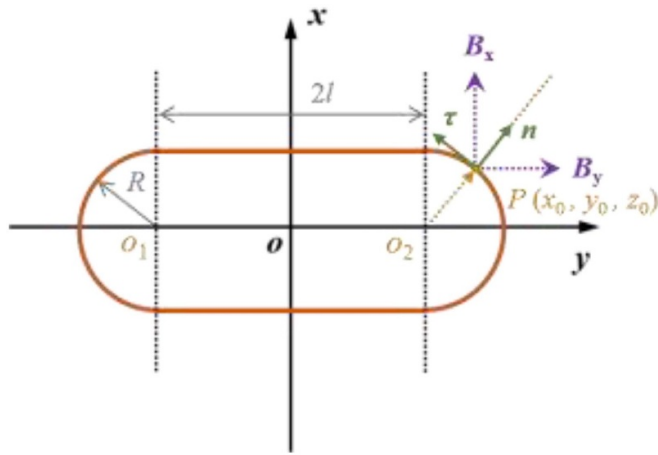


**Figure 19.** Diagram of the racetrack coil in the  $xy$ -plane.  $o_1$  and  $o_2$  are the centers of the two semicircle parts. The positive direction of the  $z$ -axis points to the inside of the paper.

and output boundaries; to keep the continuity of magnetic flux in the other boundaries, the Dirichlet boundary condition has been adopted.

It has to be noted that, the  $J_c(B)$  dependence for HTS CCs in a racetrack coil is closely linked to the angle between the magnetic field vector and the wide surface normal of the coil. We choose one racetrack coil in the  $xy$ -plane as an example, as shown in figures 19.  $2l$  and  $(R)$  are the length of the straight part and the radius of the circular part, respectively.  $\tau$  and  $n$  represent the unit tangent vector and unit normal vector at any studied point on the coil,  $P(x_0, y_0, z_0)$ .  $B_x$  and  $B_y$  denote separately the magnetic flux density components along the  $x$ -axis and  $y$ -axis. Then, the parallel and perpendicular field components can be expressed as

$$\begin{cases} \mathbf{B}_{\parallel} = (\mathbf{B}_x + \mathbf{B}_y) \cdot \tau + B_z \\ \mathbf{B}_{\perp} = (\mathbf{B}_x + \mathbf{B}_y) \cdot n \end{cases} \quad (12)$$

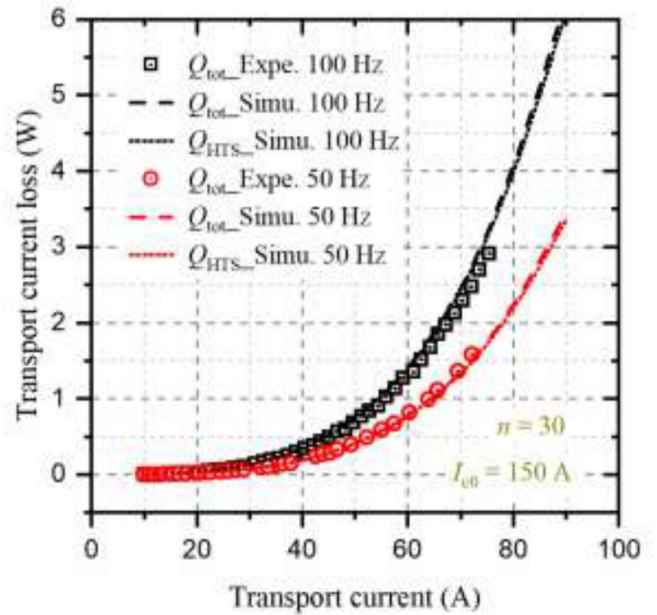


**Figure 20.** The simulated and measured transport current loss of the  $2 \times 12$  racetrack double pancake coil carrying varying AC transport current. The amplitude of the AC current varies from 10 to 90 A, and  $f$  has been chosen as 50 Hz and 100 Hz.

$$n = (n_x, n_y) = \begin{cases} \left( \frac{x_0}{\sqrt{x_0^2 + (y_0 - l)^2}}, \frac{y_0 - l}{\sqrt{x_0^2 + (y_0 - l)^2}} \right), l < y_0 \leq l + R \\ (sign(x_0), 0), -l \leq y_0 \leq l \\ \left( \frac{x_0}{\sqrt{x_0^2 + (y_0 + l)^2}}, \frac{y_0 + l}{\sqrt{x_0^2 + (y_0 + l)^2}} \right), -l - R \leq y_0 < -l \end{cases} \quad (13)$$

$$\tau = (\tau_x, \tau_y) = \begin{cases} \left( \frac{y_0 - l}{\sqrt{x_0^2 + (y_0 - l)^2}}, \frac{-x_0}{\sqrt{x_0^2 + (y_0 - l)^2}} \right), l < y_0 \leq l + R \\ (0, -sign(x_0)), -l \leq y_0 \leq l \\ \left( \frac{y_0 + l}{\sqrt{x_0^2 + (y_0 + l)^2}}, \frac{-x_0}{\sqrt{x_0^2 + (y_0 + l)^2}} \right), -l - R \leq y_0 < -l \end{cases} \quad (14)$$

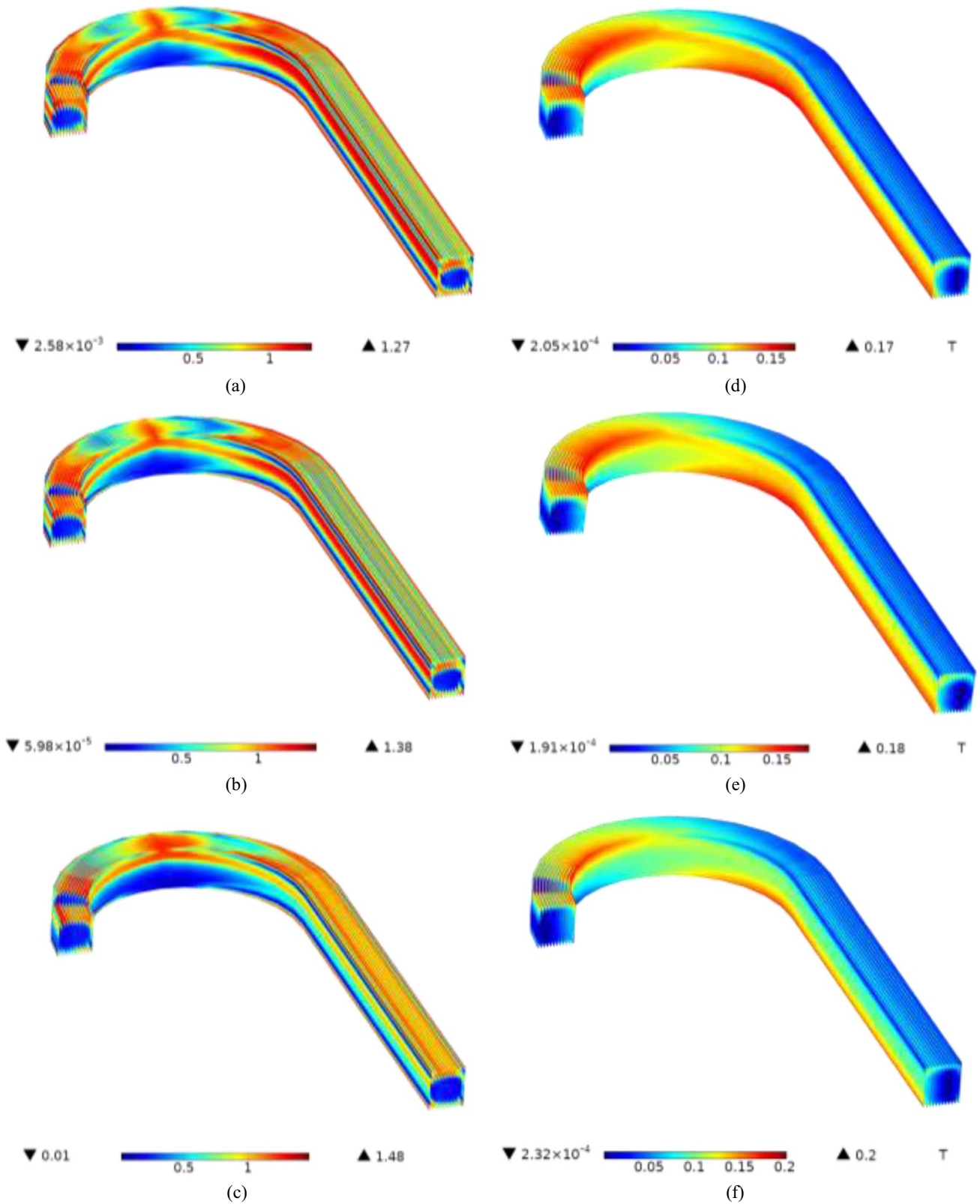


**Figure 21.** Current density and magnetic flux density distribution in the studied part of the  $2 \times 12$  racetrack double pancake coil.  $B_{\text{ext}} = 50$  mT, for each tape  $I_t = 50$  A, and  $f$  varies from 100 Hz to 10 kHz. (a), (b), and (c) present the  $J/J_c$  distribution in the HTS layer at the phase of  $2\pi$  for  $f = 100$  Hz, 1 kHz, and 10 kHz, respectively. (d), (e), and (f) show the magnetic flux density distribution at the phase of  $3\pi/2$  for  $f = 100$  Hz, 1 kHz, and 10 kHz respectively.

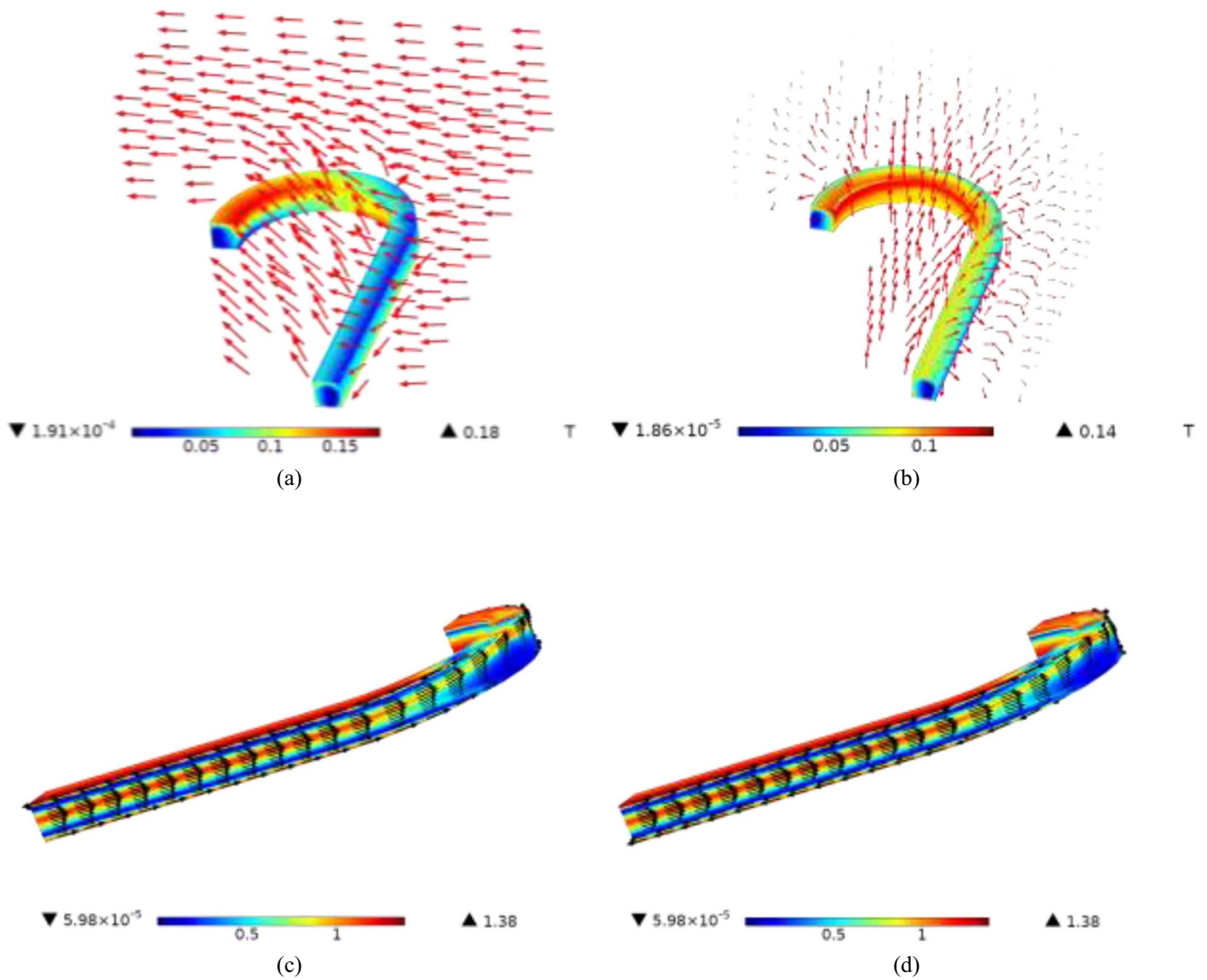


**Figure 22.** Magnetic field vector distribution in the space surrounding the studied coil part, and current vector distribution on the surface of the outermost HTS layer.  $B_{ext} = 50$  mT, for each tape  $I_t = 50$  A, and  $f = 1$  kHz. (a) and (b) present the magnetic flux distribution at the phase of  $3\pi/2$  and  $2\pi$ , respectively, inside which the red arrows represent the field vector. (c) and (d) show the current vector distribution on the surface of the outermost HTS layer at the phase of  $\pi$  and  $2\pi$ , respectively, inside which the black arrows denote the current vector.

In (12),  $\tau$  and  $n$  are actually piecewise function vectors depending on the position of the studied point  $P(x_0, y_0, z_0)$ .  $\tau$  and  $n$  can be expressed as (13) and (14), respectively.

The parameters of the tested racetrack double pancake coil studied in [28] have been adopted here. The inner radius is 10 mm, the length of the straight part is 70 mm, and the number of turns for each pancake is 12. This racetrack coil is composed of SuperOx HTS CCs, of which the self-field critical current for each CC  $I_{c0} = 150$  A at 77.4 K, and  $n = 30$ . Based on the 3D racetrack coil model, the simulated transport current loss and measured results of the whole racetrack coil at low frequencies have been depicted together in figure 20. The amplitude of transport current varies from 10 A to 90 A, and the external magnetic flux density  $B_{ext} = 0$ . It can be seen that, the simulated results are in good agreement with the experimental data. The loss generated in the HTS layer  $Q_{HTS}$  is slightly lower than the total loss  $Q_{tot}$ , thus

at low frequencies, the most loss is concentrated in the HTS layer.

Taking the  $2 \times 12$  racetrack double pancake coil as the study object, the frequency dependence of dynamic loss and magnetization loss within 100 Hz—20 kHz has been investigated. The DC transport current has been chosen as 50 A, and  $B_{ext}$  is set as 50 mT.

Figure 21 shows the current density and magnetic flux density distribution in the modelled part of the racetrack double pancake coil. (a), (b), and (c) present the  $J/J_c(B)$  distribution in the HTS layers at the phase of  $2\pi$  for  $f = 100$  Hz, 1 kHz, and 10 kHz respectively. It can be found that, with increasing frequency, the transport current is driven towards the edges of each CC, where the maximum  $J/J_c(B)$  appears and increases positively with frequency. It should be noted that, in the middle section of the circular coil part, the current density in the upper bound is much higher than that of the lower bound, which is

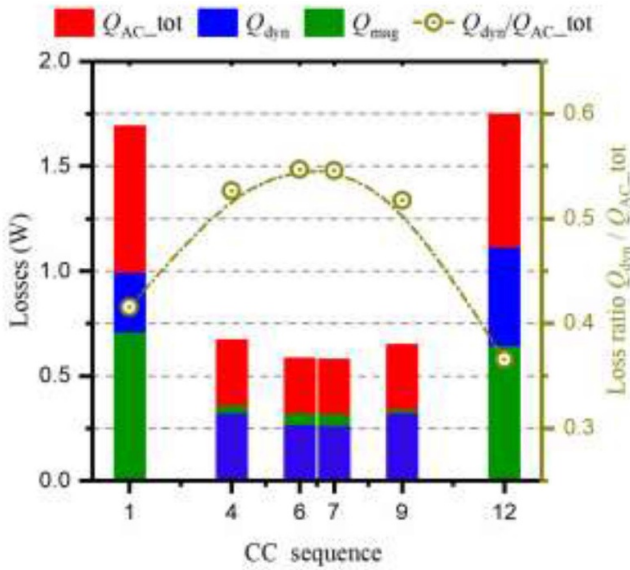


**Figure 23.** Total loss, dynamic loss and magnetization loss of the 1st, 4th, 6th, 7th, 9th and 12th double turn (from inside to outside) in the racetrack coil, when  $f = 1$  kHz,  $B_{ext} = 50$  mT, and  $I_t = 50$  A.

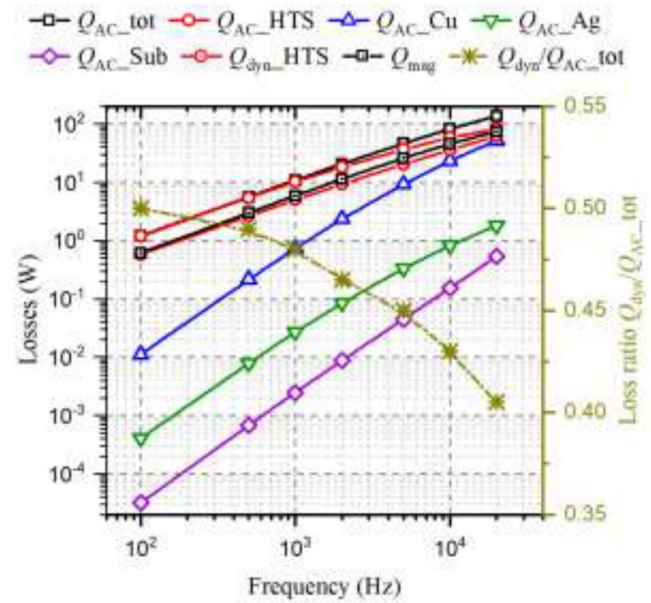


**Figure 24.** Variation of AC losses in different layers, dynamic loss magnetization loss, and loss ratio  $Q_{dyn}/Q_{AC\_tot}$  with frequency for the HTS racetrack double pancake coil.  $f$  ranges from 100 Hz to 20 kHz.  $I_t = 50$  A.  $B_{ext} = 50$  mT.

due to the occurrence of eddy current induced by the external AC magnetic field, following Lenz’s law. The skin effect at high frequencies can be seen earlier in (d), (e), and (f), inside which the magnetic flux is dragged to the edges of HTS CCs with the growth of frequency. From the cross-section of the coil, it can be found that, more magnetic flux as well as current are concentrated in the upper half compared to the lower half. This phenomenon is easy to understand because the studied part belongs to the upper pancake coil, which agrees well with the case of the double pancake circular coil in figure 15.

Taking  $f = 1$  kHz as an example, figure 22 shows the magnetic field vector distribution in the 3D space surrounding the studied coil section as well as the current vector propagation on the surface of the outermost HTS layer. Among them, (a) and (b) describe the magnetic field vector at the phase of  $3\pi/2$  and  $2\pi$ , respectively. We can see that at the phase of  $2\pi$ , the generated magnetic field (self field) is distributed symmetrically as it is only determined by the DC transport current. However, at the phase of  $3\pi/2$ , the externally applied AC magnetic field attains the peak value. In this case, the magnetic flux in the central portion of the coil is decided by both the self field and the external field, thus the direction of the field vector is towards the upper left. Figures 22(c) and (d) present the current vector distribution on the surface of the outermost HTS layer at the phase of  $\pi$  and  $2\pi$ , respectively, inside which the black arrows denote the current vector. It can be observed that, at these two moments, the middle section of the HTS layer shares the same current vector. In fact, this middle section corresponds to the dynamic region mentioned before, in which the current density is determined by the DC transport current thus the current vector remains the same direction. As a comparison, the vector directions in both edges at the two moments are opposite, which can be explained by Lenz’s law and the current gathered in the edges of the HTS layer is the eddy

current leading to magnetization loss. It should be underlined here that, figure 22 also confirms the continuity of the current and magnetic field in the corresponding boundaries, which further illustrates the effectiveness of the 3D modelling method for the pancake racetrack coil.

Figures 21 and 22 also show the shielding effect of the outermost and innermost HTS turns over the middle parts. To quantify this interaction among different layers, the total loss, dynamic loss and magnetization loss in 6 distinct double turns of the racetrack coil have been presented in figure 23, with  $f = 1$  kHz. The 6 turns are the first, fourth, sixth, seventh, ninth and twelfth double turns, respectively. It can be found clearly that, in general, there exists a higher total loss in the outermost turns and the least loss is generated in the middle turns. Besides, in the outermost CCs, the magnetization loss is much higher than the dynamic loss, however, in the middle parts, the dynamic loss accounts for the majority of the total loss. Therefore, the loss ratios  $Q_{dyn}/Q_{AC\_tot}$  attain the highest value at the 6th and 7th turns, which are all beyond 50%, and becomes the smallest at the 12th one. To conclude, the outer turns have an evident shielding effect over the inner parts of the racetrack coil, and the shielding effect enhances the significance of dynamic loss, which agrees well with the conclusions drawn from the case of the circular coil. Thence, we need to realize that, even at high frequencies of kHz level, dynamic loss can still dominate the total power dissipation in the middle turns of racetrack coils.

It should be pointed out that, in figure 16 the total loss of each turn of the circular coil increases from the inside out, which is different from figure 23. In fact, the modelling of the circular coil is based on a 2D method, in which the externally applied magnetic field is centrosymmetric as described in

[32], thus the shielding effect on the inner parts is from the outermost turn. However, the modelling of the racetrack coil here is a 3D method, and the externally applied magnetic field is not centrosymmetric, thus both the innermost and outermost turns share the shielding effect on the middle ones. From this point of view, it can only be achieved by 3D modelling methods to set a complex spatial magnetic field based on different boundary conditions, which is a distinguished advantage over 2D numerical models.

Figure 24 describes the variation of the AC losses in different layers, dynamic loss as well as magnetization loss in the racetrack double pancake coil. Generally, figure 24 shows the same trend as figures 17 and 12, that the total loss, the magnetization loss and the loss generated in the copper stabilizers increase rapidly with frequency due to the skin effect. The magnetization loss becomes greater than the dynamic loss for frequencies higher than 200 Hz, and the loss ratio  $Q_{\text{dyn}}/Q_{\text{AC\_tot}}$  drops from 51% at 100 Hz to approximately 40% at 20 kHz. Therefore, in the studied frequency range, the magnetization loss generally plays a dominant role, however, the portion of dynamic loss over the total loss remains above 45% within the frequency band below 3 kHz. Hence, as concluded in Section 3.3.1, both dynamic loss and magnetization loss are significant for the HTS racetrack coils operated in a high-speed synchronous machine.

#### 4. Conclusions

In this paper, through an **H**-formulation based numerical modelling method, the frequency dependence of dynamic loss and magnetization loss for an HTS CC, a stack, a circular double pancake coil as well as a racetrack double pancake coil over a wide range, from 100 Hz to 20 kHz has been systematically investigated. The adopted numerical multilayer models have taken into account the physical structure of a CC, namely the copper stabilizers, HTS layer, silver overlayer as well as substrate, which have been validated by multiple experimental measurements from other published work.

The existing definition of the dynamic region and analytical equations for calculating dynamic loss have been found to be not applicable at the kHz level, in that the dynamic region of a single CC shrinks rapidly with increasing frequency and the skin effect results in a redistribution of magnetic flux and current among different layers. Therefore, the **H**-formulation based numerical multilayer model has been proposed to quantify the dynamic loss and magnetization loss. Afterward, the correlation between dynamic loss, magnetization loss, and the total loss has been discussed in detail.

(1) In general, magnetization loss per unit time is in a positive correlation with frequency. Under skin effect, both current and magnetic flux inside the CC will be driven to both ends and outer copper stabilizers with increasing frequency, thus the losses in the copper stabilizers will be approaching magnetization loss as well as the total loss.

(2) There exists a positive correlation between dynamic loss and frequency followed by a negative one because at higher frequencies the amount of traversing magnetic flux during

one AC cycle shrinks rapidly. For example, the peak value of dynamic loss appears at  $f = 10$  kHz for the studied stack with  $i = 0.5$  and  $B_{\text{ext}} = 20$  mT.

(3) At low frequencies, dynamic loss occupies the majority of the total AC loss for HTS CCs, stacks and coils. For example, when  $f = 100$  Hz,  $I_t = 50$  A and  $B_{\text{ext}} = 50$  mT, the loss ratio between dynamic loss and total loss of the double pancake racetrack coil is above 50%. However, as the frequency increases, the magnetization loss becomes more important due to skin effect, indicated by a reduction in the loss ratio to 40% at 20 kHz.

(4) At low frequencies, *e.g.*  $f = 100$  Hz, a higher  $B_{\text{ext}}$  leads to a higher dynamic loss because of more magnetic flux traversing the HTS CC. However, at higher frequencies above 1 kHz, a higher  $B_{\text{ext}}$  results in a higher magnetization loss due to skin effect and the loss contribution from copper stabilizers.

(5) Compared with a single CC, the influence of dynamic loss in HTS stacks or coils is more significant because the shielding effect among different turns can enhance the significance of dynamic loss, bringing about a higher magnetization loss ratio in the outermost turns and a higher dynamic loss proportion in the middle parts.

To conclude, under the skin effect and shielding effect, both dynamic loss and magnetization loss should be attached to high importance for the design of HTS magnets and machine windings operated in a high-frequency environment, *e.g.* at the kHz level or even higher. For quantifying the loss characteristics over a wide frequency range, the numerical multilayer model considering the physical CC structure has to be used. With respect to modelling of HTS racetrack coils carrying transport current under varying magnetic fields, the 3D numerical model is recommended with different boundary conditions, so that a complex external magnetic field can be applied. This paper can be used for accurate loss controlling in HTS machine windings and magnets operated in a high-frequency environment, providing some reference for the design of future aerospace electric propulsion systems.

It should be underlined that, this work concentrates on the electromagnetic characteristics of HTS windings applied in high-speed machines. Therefore, the field dependence of critical current of HTS CCs has been considered and we assume that the cooling power of the cryocooler is sufficient to remove the heat dissipation in the coils instantaneously. In this case, the temperature dependence of critical current and the overall design of cryogenic systems have not been considered in this paper. However, the predicted loss distribution and quantified loss level provide a reference to the overall design of highly efficient cryogenic systems. In the future, more research should be carried out to explore the thermal properties of HTS windings and the design of highly efficient cryocoolers for aerospace machines.

#### Acknowledgments

This work was supported by the joint scholarship from the University of Edinburgh and China Scholarship Council (CSC) under Grant [2018] 3101. The authors kindly thank Dr

Zhenan Jiang for the dynamic loss measurement of the HTS CC. Hongye Zhang would like to thank Dr Yu Cao (Institute for Energy Systems at the University of Edinburgh) for his help in computing skills.

## ORCID iDs

Hongye Zhang  <https://orcid.org/0000-0002-8960-4614>  
 Philip Machura  <https://orcid.org/0000-0002-2709-4575>  
 Kevin Kails  <https://orcid.org/0000-0002-3418-5977>  
 Hongyi Chen  <https://orcid.org/0000-0002-6232-5463>

## References

- [1] Schäfer A W, Barrett S R H, Doyme K, Dray L M, Gnadt A R, Self R, O'Sullivan A, Synodinos A P and Torija A J 2019 Technological, economic and environmental prospects of all-electric aircraft *Nat. Energy* **4** 160–6
- [2] Zhang X, Bowman C L, O'Connell T C and Haran K S 2018 Large electric machines for aircraft electric propulsion *IET Electr. Power Appl.* **12** 767–79
- [3] Durrell J H, Ainslie M D, Zhou D, Vanderbemden P, Bradshaw T, Speller S, Filipenko M and Cardwell D A 2018 Bulk superconductors: A roadmap to applications *Supercond. Sci. Technol.* **31** 103501
- [4] Kim H D, Perry A T and Ansell P J 2018 A review of distributed electric propulsion concepts for air vehicle technology *AIAA/IEEE Electric Aircraft Technologies Symp. (EATS)* July 2018 pp 1–21
- [5] Haran K S *et al* 2017 High power density superconducting machines—Development status and technology roadmap *Supercond. Sci. Technol.* **30** 123002
- [6] Liu Y *et al* 2019 Dynamic resistance measurement in a YBCO wire under perpendicular magnetic field at various operating temperatures *J. Phys. D: Appl. Phys.* **126** 243904
- [7] Jiang Z, Hamilton K, Amemiya N, Badcock R A and Bumby C W 2014 Dynamic resistance of a high- $T_c$  superconducting flux pump *Appl. Phys. Lett.* **105** 112601
- [8] Ainslie M D, Bumby C W, Jiang Z, Toyomoto R and Amemiya N 2018 Numerical modelling of dynamic resistance in high-temperature superconducting coated-conductor wires *Supercond. Sci. Technol.* **31** 074003
- [9] Kails K, Zhang H, Machura P, Mueller M and Li Q 2020 Dynamic loss of HTS field windings in rotating electric machines' *Supercond. Sci. Technol.* **33** 045014
- [10] Coombs T A 2019 Superconducting flux pumps *J. Phys. D: Appl. Phys.* **125** 230902
- [11] Kails K *et al* 2020 Loss characteristics of HTS coated conductors in field windings of electric aircraft propulsion motors *Supercond. Sci. Technol.* **33** 064006
- [12] Oomen M P, Rieger J, Leghissa M, Ten Haken B and Ten Kate H H J 1999 Dynamic resistance in a slab-like superconductor with  $J_c(B)$  dependence *Supercond. Sci. Technol.* **12** 382–7
- [13] Zhang H, Yao M, Jiang Z, Xin Y and Li Q 2019 Dependence of dynamic loss on critical current and  $n$ -value of HTS coated conductors *IEEE Trans. Appl. Supercond.* **29** 1–7
- [14] Zhang H, Chen H, Jiang Z, Yang T, Xin Y, Mueller M and Li Q 2020 A full-range formulation for dynamic loss of HTS coated conductors *Supercond. Sci. Technol.* **33** 05LT01
- [15] Jiang Z, Toyomoto R, Amemiya N, Zhang X and Bumby C W 2017 Dynamic resistance of a high- $T_c$  coated conductor wire in a perpendicular magnetic field at 77 K *Supercond. Sci. Technol.* **30** 03LT01
- [16] Duckworth R C, Zhang Y F, Ha T and Gouge M J 2011 Dynamic resistance of YBCO-coated conductors in applied ac fields with dc transport currents and DC background fields *IEEE Trans. Appl. Supercond.* **21** 3251–6
- [17] Jiang Z, Toyomoto R, Amemiya N, Bumby C W, Badcock R A and Long N J 2017 Dynamic resistance measurements in a GdBCO-coated conductor *IEEE Trans. Appl. Supercond.* **27** 1–5
- [18] Jiang Z *et al* 2018 Dynamic resistance measurement of a four-tape YBCO stack in a perpendicular magnetic field *IEEE Trans. Appl. Supercond.* **28** 1–5
- [19] Zhang H, Yao M, Kails K, Machura P, Mueller M, Jiang Z, Xin Y and Li Q 2020 Modelling of electromagnetic loss in HTS coated conductors over a wide frequency band *Supercond. Sci. Technol.* **33** 025004
- [20] Amemiya N, Murasawa S, Banno N and Miyamoto K 1998 Numerical modelings of superconducting wires for loss calculations *Phys. C* **310** 16–29
- [21] Rodriguez-Zermeno V M *et al* 2011 Towards faster FEM simulation of thin film superconductors: a multiscale approach *IEEE Trans. Appl. Supercond.* **21** 3273–6
- [22] Zhou P *et al* 2019 Transition frequency of transport ac losses in high temperature superconducting coated conductors *J. Phys. D: Appl. Phys.* **126** 063901
- [23] Zhang M and Coombs T A 2012 3D modeling of high- $T_c$  superconductors by finite element software *Supercond. Sci. Technol.* **25** 015009
- [24] Rhyner J 1993 Magnetic properties and ac-losses of superconductors with power law current-voltage characteristic *Phys. C* **212** 292–300
- [25] Zermeno V M R and Grilli F 2014 3D modeling and simulation of 2G HTS stacks and coils *Supercond. Sci. Technol.* **27** 044025
- [26] Matsushita T 1994 *Flux Pinning and Electromagnetic Phenomenon* (Tokyo, Japan: Sangyo Tosho, Inc.)
- [27] Mikitik G P and Brandt E H 2001 Generation of a dc voltage by an ac magnetic field in type II superconductors *Phys. Rev. B* **64** 092502
- [28] Zubko V, Fetisov S, Zanegin S and Vysotsky V, 'AC losses analysis in stack of 2G HTS tapes in a coil', *TechRxiv*, Preprint. [10.36227/techrxiv.11635320.v1](https://arxiv.org/abs/10.36227/techrxiv.11635320.v1)
- [29] Shen B, Li C, Geng J, Zhang X, Gawith J, Ma J, Liu Y, Grilli F and Coombs T A 2018 Power dissipation in HTS coated conductor coil under the simultaneous action of AC and DC currents and fields *Supercond. Sci. Technol.* **31** 075005
- [30] Machura P, Zhang H, Kails K and Li Q 2020 Loss characteristics of superconducting pancake, solenoid and spiral coils for wireless power transfer *Supercond. Sci. Technol.* accepted [10.1088/1361-6668/ab931d](https://doi.org/10.1088/1361-6668/ab931d)
- [31] Zermeno V M R, Abrahamsen A B, Mijatovic N, Jensen B B and Sørensen M P 2013 Calculation of alternating current losses in stacks and coils made of second generation high temperature superconducting tapes for large scale applications *J. Phys. D: Appl. Phys.* **114** 173901
- [32] Ainslie M D, Hu D, Zou J and Cardwell D A 2015 Simulating the in-field AC and DC performance of high-temperature superconducting coils *IEEE Trans. Appl. Supercond.* **25** 1–5